RSC Advances

PAPER

View Article Online
View Journal | View Issue

Cite this: *RSC Adv.*, 2021, **11**, 4942

N/Fe/Zn co-doped TiO_2 loaded on basalt fiber with enhanced photocatalytic activity for organic pollutant degradation

Lingxiao Yang,[b] Lanmiao Li,[b] Longguo Li,[ab] Chao Liu,[ab] Jun Li,[ab] Bo Lai *[ac] and Naiwen Li *[ab]

To avoid the loss of catalytic material powder, a loaded catalytic material of TiO_2 with basalt fiber as the carrier (TiO_2@BF) was synthesized by an improved sol–gel method. The TiO_2@BF was doped with different contents of N, Fe and Zn elements and was used to degrade rhodamine B (RhB) under ultraviolet light. The physical characterization analysis indicated that the co-doping of the N, Fe and Zn elements had the effects of reducing grain size, increasing sample surface area, and narrowing the electronic band gap. The electronic band gap of nitrogen–iron–zinc co-doped TiO_2@BF (N/Fe/Zn_TiO_2@BF) was 2.80 eV, which was narrower than that of TiO_2@BF (3.11 eV). The degradation efficiency of RhB with N/Fe/Zn_TiO_2@BF as a photocatalyst was 4.3 times that of TiO_2@BF and its photocatalytic reaction was a first-order kinetic reaction. Quenching experiments suggested that the reactive species mainly include photoinduced holes (h^+), superoxide radicals ($^{\bullet}O_2^-$) and hydroxyl radicals ($^{\bullet}OH$). In brief, this study provides a prospective loaded catalytic material and routine for the degradation of organic contaminants in water by a photocatalytic process.

Received 30th November 2020
Accepted 12th January 2021

DOI: 10.1039/d0ra10102h

rsc.li/rsc-advances

1 Introduction

At present, water pollution caused by man-made organic pollutants has become one of the key concerns all over the world.[1–4] Large quantities of organic compounds, such as synthetic dyes and endocrine disruptors, originating from industries including textiles, plastics, pharmaceuticals, *etc.*,[5,6] would have harmful effects on mankind and animal life in short or long periods of time. Water pollution caused by dye wastewater discharged from traditional industries, one of the most common contaminants, has attracted extensive attention.[7] Rhodamine B (RhB), a typical pollutant of dye molecules,[8] is difficult to be removed by self-purification of natural water systems because of its high stability and it greatly threatens human health due to its toxicity. Therefore, research into removing dye molecules in water has become a hot topic in recent years.

Nowadays, common water treatment methods mainly include membrane filtration,[9] coagulation sedimentation,[10] electrochemical,[11] advanced oxidation process,[12,13] and biological treatment[14] methods. Photocatalytic oxidation, an advanced oxidation process, could efficiently eliminate various harmful organic compounds. It has attracted extensive attention in the field of water environmental protection and restoration due to the advantages of low cost, easy operation, high efficiency, low consumption, no secondary pollution, and great damage to dye molecules.

In the study of photocatalytic oxidation to degrade pollutants, TiO_2 nanoparticles[15] are one of the most widely studied semiconductor photocatalysts in photocatalysis due to their strong oxidizing ability, chemical stability, safety, non-toxicity, and high photocatalytic potential.[16,17] However, TiO_2 has some intrinsic drawbacks in practical applications such as its wide band gap and charge carrier recombination, which result in low light utilization efficiency and photocatalytic activity in the visible region.[18,19] Consequently, tremendous efforts have been devoted to improving the photocatalytic efficiency of TiO_2 *via* modification, including doping modification,[20] surface modification,[21] dye sensitization,[22] deposition of noble metals,[23,24] semiconductor recombination,[25] *etc.* In particular, metal doping[26] and non-metal doping[27] for TiO_2 have proved to be the most effective methods and have been extensively studied.

In addition, TiO_2 nanoparticles are difficult to recycle and reuse in applications because of their small particles. In order to solve the problem of catalyst recycling and reuse, many researchers have used different substances as carriers to support TiO_2 to synthesize TiO_2 loaded composites, such as activated carbon, glass fiber and carbon fiber.[28–30] Basalt fiber

[a]State Key Laboratory of Hydraulics and Mountain River Engineering, Sichuan University, Chengdu, Sichuan 610065, China. E-mail: linaiwen@scu.edu.cn; laibo@scu.edu.cn
[b]College of Water Resource & Hydropower, Sichuan University, Chengdu, Sichuan 610065, China
[c]Sino-German Centre for Water and Health Research, Sichuan University, Chengdu 610065, China

(BF) is made of pure natural basalt ore as the raw material and its main component is SiO_2, which has a similar structure to TiO_2. Therefore, BF, which has similar mineral properties to TiO_2, could adhere to TiO_2 firmly. Generally, to synthesize TiO_2 loaded composites, TiO_2 nanoparticles need to be prepared first and then dispersed in a sol to carry out loading. The high temperature resistance and excellent physicochemical stability of BF allows it to be loaded in the intermediate step of TiO_2 preparation and then calcined to obtain the composite material in one step, thereby increasing the loading efficiency of TiO_2 and saving time and cost. To the best of our knowledge, no studies on TiO_2 loaded on BF for the degradation of organic contaminants in water have been reported.

In the current study, a new three-dimensional structure model was made from BF and TiO_2 with three doping elements of N, Fe, and Zn loaded on the BF to prepare a multi-element co-doped TiO_2@BF composite material, which has a larger contact area with water and a higher light transmittance. The synthesized new multi-element doped G_TiO_2@BF (in G_TiO_2@BF, G represents the dopants N, Fe and Zn) composite material was characterized. Meanwhile, the doping substance combination and the effects of the dopant content (%) of different dopants were investigated, the photocatalytic performance of the synthesized material was tested for the degradation of RhB and the possible degradation mechanisms were studied.

2 Experimental materials and methods

2.1 Chemical reagents

Tetrabutyl titanate (≥98.5%), ethyl alcohol (≥99.5%, anhydrous), and nitric acid (65–68%) were used for TiO_2 synthesis. Urea (≥99.0%), ZnO (≥98.0%), and ferric nitrate nonahydrate (≥98.5%) were used as reagents when doping and modifying TiO_2. Rhodamine B (RhB) was used in the photocatalytic degradation experiment. 1,4-Benzoquinone (BQ, ≥98.5%), *tert*-butyl alcohol (TBA, ≥99.0%) and EDTA-2Na (≥99.0%) were used in the reactive species quenching experiments. All the reagents were from Chron Chemicals Co., Ltd. (Sichuan, China). Distilled water (resistance > 18.25 MΩ), used in all experiments, was provided by a water purification system (ULUPURE, China).

2.2 Synthesis of the catalytic loaded composites

2.2.1 Colloidal sol. Typically, 200 mL of tetrabutyl titanate was added dropwise to a 1000 mL sized beaker containing 600 mL ethyl alcohol with constant mechanical stirring. After mixing, 30 mL of nitric acid was added to the mixture slowly and uniformly, then the beaker was sealed and stirring continued for 1 hour. Finally, a yellow transparent sol was obtained.

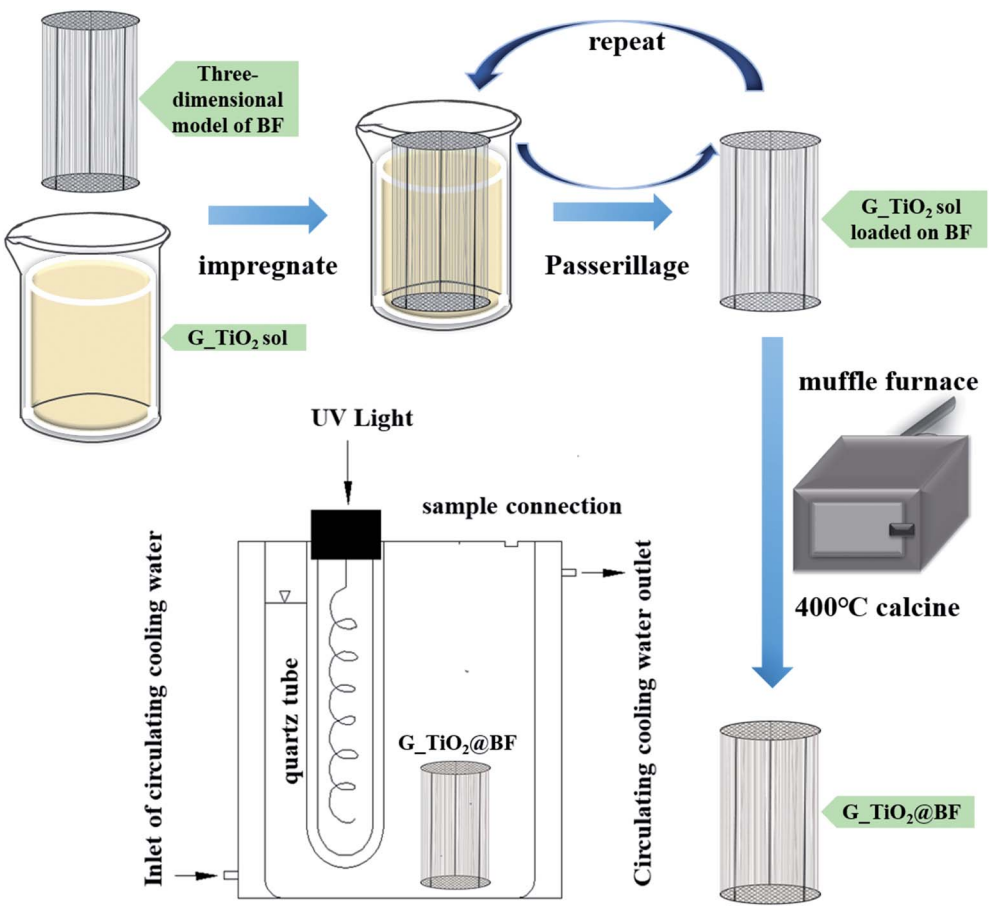

Fig. 1 Preparation steps of G_TiO_2@BF and the photocatalytic degradation reaction device.

2.2.2 Doping. N_TiO_2 sol, Fe_TiO_2 sol and Zn_TiO_2 sol were synthesized, respectively, doping substances of urea, ferric nitrate nonahydrate and ZnO with different doping ratios. The corresponding proportions were n(N) : n(Ti) = (6%, 8%, and 12%), n(Fe) : n(Ti) = (0.03%, 0.3%, and 1%), and n(Zn) : n(Ti) = (0.5%, 2%, and 7%). The doping substances with different doping ratios were separately dissolved in 600 mL ethyl alcohol and then the mixed solution was used as an organic solvent. The remaining steps were consistent with the preparation of the sol. After the photocatalytic degradation of RhB with single doping of TiO_2@BF, the optimal doping ratio was selected to be 8% N, 0.3% Fe and 2% Zn, and then the three materials were co-doped with an optimal doping ratio of N, Fe, and Zn to obtain the N/Fe/Zn_TiO_2 sol.

2.2.3 Catalytic loaded composites. After the sol was prepared, the three-dimensional model of BF shown in Fig. 1 was evenly loaded with a layer of sol by the dipping method and the second impregnation was carried out after the first layer was naturally air-dried. After that, the BF model was placed in a drying oven at a temperature of 85 °C for 50 minutes to volatilize the ethyl alcohol, then put in a muffle furnace at 400 °C and calcined for 3 hours. Finally, TiO_2@BF, N_TiO_2@BF, Fe_TiO_2@BF, Zn_TiO_2@BF and N/Fe/Zn_TiO_2@BF were obtained. The TiO_2 loading quantity was calculated by the mass difference between the three-dimensional model of BF without loading TiO_2 and TiO_2@BF.

Fig. 1 presents the preparation steps of loading TiO_2 on BF and the photocatalytic degradation reaction device. The BF model was based on a round wire mesh as a fiber guide bracket; three equal-height wires were used as a wire mesh fixed bracket and 126 basalt fiber bundles were fixed at 5 mm intervals on it. Every basalt fiber bundle was 27 cm in length and 0.5 mm in diameter.

2.3 Characterization

The surface morphology and fracture morphology of the sample were examined by scanning electron microscopy (SEM, S-450, Japan). Energy dispersive spectrometry (EDS, Aztec X-Max80, UK) was applied to the qualitative analysis of elements. The crystalline phases and grain size of the samples were characterized by X-ray diffraction (XRD, EMPYREAN, UK), using Cu Kα radiation ($\lambda_1 = 1.5406$ Å, $\lambda_2 = 1.5444$ Å), a monochromatic slit of 0.76 mm, a 2θ diffraction angle of 10° to 80° and a scan step of 0.03° s^{-1}. The functional groups were analyzed by Fourier transform infrared spectroscopy (FT-IR, Nicolet 6700, USA). The molecular structural groups were analyzed by Raman spectra (RAMAN, LabRAM HR800, France). The surface composition and chemical state of the sample were investigated by the AXIS

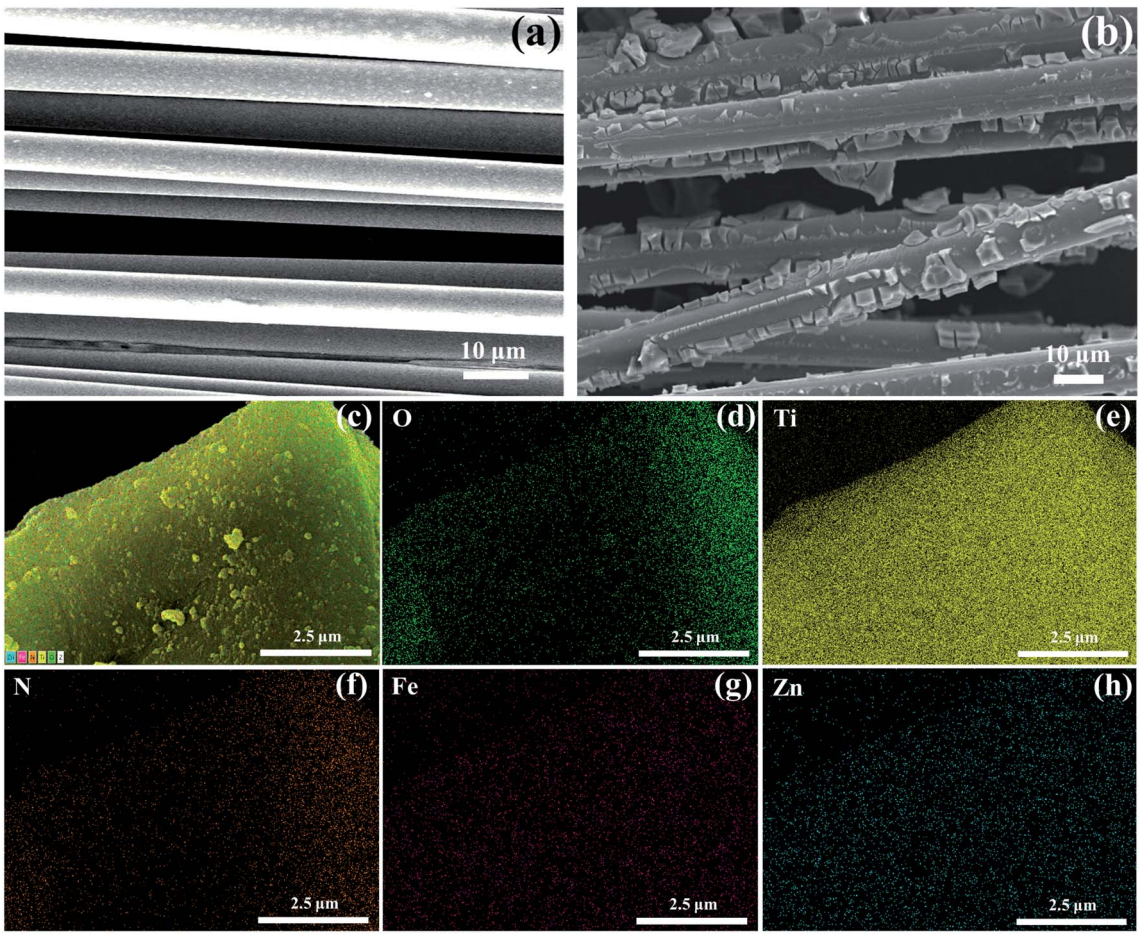

Fig. 2 SEM micrographs for the samples: (a) BF and (b) TiO_2@BF; EDS elemental mapping images of (c)–(h) N/Fe/Zn_TiO_2@BF.

Supra multifunctional X-ray photoelectron spectrometer (XPS, KRATOS, UK), using a monochromatic X-ray source. The electronic band gaps of the synthesized photocatalysts were analyzed by UV-visible diffuse-reflectance spectroscopy (UV-vis/DRS, UV-3600, Japan). The samples used for characterization like TiO_2 refer to powders scratched off from the fiber and those like TiO_2@BF refer to layers loaded on basalt fibers.

2.4 Photocatalytic degradation of RhB

The photocatalytic degradation of RhB was investigated under ultraviolet (UV) light in a photocatalytic dark box reactor. The experiments were performed in a 10 L cylindrical black box with a mercury lamp (42 W, $\lambda = 235.7$ nm) as the light source, and circulating water was adopted to control the reaction temperature at ambient temperature. In order to eliminate the disturbance of the adsorption, it is necessary to reach an adsorption/desorption equilibrium before turning on the light.[31] After the samples of G_TiO_2@BF (G represents the dopant) were added into 7 L RhB solution (5 mg L^{-1}) for 30 min in the dark, the experiment was kept for 180 min under UV light. During the experiment, 50 mL of RhB solution was sampled at certain intervals and the supernatant solution was obtained at high-speed centrifugation before detecting the RhB concentration by spectrophotometry (V729, YOKE INSTRUMENT, China) at 554 nm. The degree of RhB degradation was expressed as C_t/C_0, where C_t was the RhB concentration at the sampling time, and C_0 was RhB concentration at the initial time. The stability and reusability experiment materials were washed with absolute ethanol and deionized water several times. The samples were calcined at 400 °C for 1 h before the next cycle experiment was carried out.

3 Results and discussion

3.1 Physicochemical properties

3.1.1 Crystal structure, crystallite size and morphology. The photocatalytic activity is greatly influenced by the crystal phase of TiO_2. As reported, the photocatalytic activity of anatase phase TiO_2 synthesized at 400 °C is better than that of the rutile phase and brookite phase.[32,33] Therefore, 400 °C was selected as the calcination temperature to prepare the catalyst.

Fig. 2(a) and (b) depict the microstructure and morphology of BF and TiO_2@BF by SEM, from which it could be obviously observed that the fibers were wrapped with TiO_2. There were many micropores on the surface of the synthesized N/Fe/Zn_TiO_2@BF catalyst due to using urea as the N doping source. During the calcination process, urea could change to gas and escape, increasing the specific surface area of material. As shown in Fig. 2(c)–(h), it was confirmed that the O, Ti, N, Fe and Zn elements coexisted on the N/Fe/Zn_TiO_2@BF.

XRD is performed to characterize the crystal structure of the material. TiO_2 was stripped from the BF surface to analyze its crystal phase due to the diffraction peak of BF covering that of TiO_2. Fig. 3 depicts the XRD results of the synthesized TiO_2 and N/Fe/Zn_TiO_2 and TiO_2@BF. The diffraction peak of synthesized TiO_2 appeared at $2\theta = 25.22°$ (101), 37.89° (004), 48.07° (200), 53.81° (105), 55.08° (211) and 62.63° (204), which

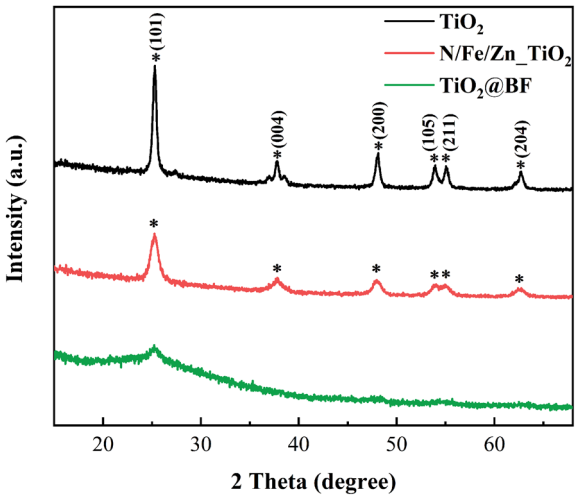

Fig. 3 XRD spectra of TiO_2, N/Fe/Zn_TiO_2 and TiO_2@BF prepared at 400 °C.

matched well with the JCPDS NO: 21-1272. The result shows that the synthesized TiO_2 was monocrystalline and in the pure anatase phase, which was confirmed by there being no diffraction peaks at $2\theta = 27.5°$ (110) and 30.8° (121), corresponding to the rutile and brookite phase. The diffraction peak location of N/Fe/Zn_TiO_2 also corresponded to the anatase phase, indicating that the doping of N, Fe and Zn did not change the crystal structure of pristine TiO_2. In addition, the XRD spectra of N/Fe/Zn_TiO_2 (Fig. 3) show no peaks of Zn oxide and Fe oxide.

The crystallite sizes were calculated from the stretching of the anatase (101) peaks by using the Scherrer formula as follows.

$$D = k\lambda/\beta \cos\theta \quad (1)$$

where D is the crystallite size (nm), k is the Scherrer constant (0.89), λ is the wavelength of X-ray (1.5406 Å), β is the half-height width of the diffraction peak of the measured sample (rad), and θ is the Bragg diffraction angle (°). The crystallite size of synthesized TiO_2 and N/Fe/Zn_TiO_2 was calculated to be 18.1 nm and 10.4 nm, respectively, which indicated that the doping of N/Fe/Zn affects the crystallite size. With the smaller particles and bigger specific surface area, the catalysts would provide more catalytic activity points, and catalytic efficiency was improved. The result that N/Fe/Zn_TiO_2 had a wider diffraction peak and a smaller relative peak strength than TiO_2 (Fig. 3) also proves that the dopant would inhibit crystal growth. A similar result was also obtained by Ebrahim Rezaei.[29]

As shown in Fig. 4(a), it was difficult to observe the vibration modes of TiO_2 and N/Fe/Zn_TiO_2 due to the diffraction peak of BF covering that of TiO_2 in the RAMAN spectra of the synthesized TiO_2@BF and N/Fe/Zn_TiO_2@BF. As displayed in Fig. 4(b), their TiO_2 crystals were both in the anatase phases. As could be seen from Fig. 4(b), the positions of the characteristic bands in the synthesized TiO_2 of 143.2, 197, 395.4, 515 and 639 cm^{-1} correspond to the vibration modes of E_g, E_g, B_{1g}, A_{1g} and E_g in

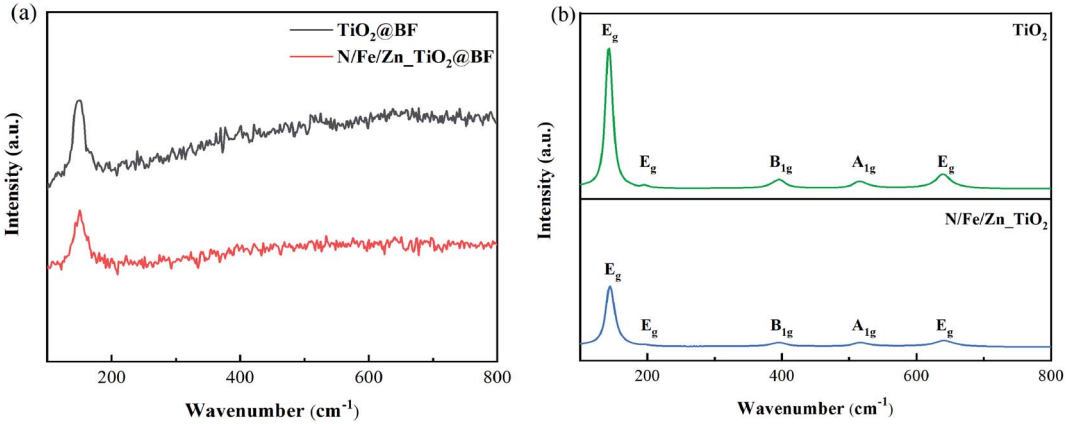

Fig. 4 RAMAN spectra of (a) TiO_2@BF and N/Fe/Zn_TiO_2@BF and (b) TiO_2 and N/Fe/Zn_TiO_2 prepared at 400 °C.

the single crystal anatase phase, respectively. The result that only five vibration modes appeared was lower than the six Raman activation modes ($A_{1g} + 2B_{1g} + 3E_g$) reported by Ohsaka[34] because the peaks at positions 513 and 515 cm^{-1} overlap; a similar result was also obtained by Choi[35] and Cho.[36] In Fig. 4(b), no characteristic bands were observed at 445 and 612 cm^{-1}, indicating that the rutile phase did not exist in the prepared TiO_2 sample. Compared with the characteristic peaks of TiO_2, the characteristic peaks of N/Fe/Zn_TiO_2 were weakened and the half-peak width increased due to the decrease of crystallinity size after doping, which was consistent with the XRD results.

3.1.2 Chemical state, electronic structure and electronic band gaps. The chemical composition of the surface of TiO_2@BF and N/Fe/Zn_TiO_2@BF was determined by XPS, as shown in Fig. 5. Compared with the full XPS spectrum of TiO_2@BF (Fig. 5(a)), the characteristic peaks of Zn and N appeared in the full XPS spectrum of N/Fe/Zn_TiO_2@BF (Fig. 5(b)) but the Fe signal was not detected due to the low content of Fe in N/Fe/Zn_TiO_2@BF. The Zn 2p core spectrum in Fig. 5(c) shows that the peaks of 1045.08 eV and 1021.97 eV correspond to Zn $2p_{1/2}$ and Zn $2p_{2/3}$, respectively, indicating that Zn in N/Fe/Zn_TiO_2@BF had *a* +2 valence.[37] Meanwhile, all Zn exist in the Zn^{2+} state and Zn $2p_{3/2}$ bonds or coordinates with oxygen.[38] Fig. 5(d) shows a peak at 401.22 eV of the N 1s core spectrum of N/Fe/Zn_TiO_2@BF from the Gaussian fitting curve, indicating that N was oxidized to form a Ti–O–N bond.[39] In Fig. 5(e), it could be seen that the binding energy values were 464.22 eV and 458.48 eV, belonging to Ti $2p_{1/2}$ and Ti $2p_{3/2}$, respectively, indicating the appearance of Ti^{4+}.[40,41] As shown in Fig. 5(f), the co-doping of N, Fe and Zn did not change the valence state of Ti, which was still in the valence state of Ti^{4+}. As observed in Fig. 5(g), the O 1s spectra of TiO_2 could be divided into two peaks at 529.76 eV and 539.72 eV, corresponding to Ti–O–Ti and surface defects or surface hydroxy-groups, respectively.[42] In Fig. 5(h), the co-doping did not change the state of O 1s.

The real doping contents for N/Fe/Zn_TiO_2@BF were calculated from the quantitative method of the XPS sensitivity factor by using the following formula.

$$C_x = (A_x/S_x)/(\Sigma A_i/S_i) \quad (2)$$

where C_x is the concentration of the element at the surface, A_x is the XPS peak area of the desired element, S_x is the relative sensitivity factor of the XPS peak (the RSF of N 1s, Zn 2p and Ti 2p is 0.477, 5.589 and 2.001, respectively), $\Sigma A_i/S_i$ is the sum of the ratio of the peak area to the relative sensitivity factor of all the measured elements. The XPS peak area values of N 1s, Zn 2p and Ti 2p were 141.55, 2466.49 and 26 432.85, obtained from the XPS spectrum of N/Fe/Zn_TiO_2@BF. When the concentration ratio was obtained, the molar ratio could be further calculated to be n(N) : n(Ti) = 8% and n(Zn) : n(Ti) = 2%. The Fe peak was not detected due to the low Fe content in N/Fe/Zn_TiO_2@BF. The real doping content of N/Fe/Zn_TiO_2@BF obtained through the XPS analysis was the same as the theoretical doping content.

The FT-IR spectra of the synthesized TiO_2 and N/Fe/Zn_TiO_2 are shown in Fig. 6, which was used to analyze the functional groups of the samples. In Fig. 6(a), the peaks at 3439 cm^{-1} and 1630 cm^{-1} were formed by the stretching vibration of the water adsorbed on the surface, $^{\bullet}$OH or the H–OH bond of the COOH group, and the peak at 513 cm^{-1} was attributed to the characteristic Ti–O bond vibration of TiO_2.[43,44] In Fig. 6(b), compared with Fig. 6(a), there was a slight offset value at the characteristic peak of TiO_2 and the absorption peak of the hydroxyl group. Combined with the results of the XRD and XPS, it indicated that N, Fe and Zn entered into the lattice of TiO_2.

3.2 Photocatalytic degradation of RhB

As shown in Fig. 7(a), RhB removal by TiO_2 (17.93%) alone was a little better than that of TiO_2@BF (15.61%), which was due to the TiO_2 in TiO_2@BF being wrapped, leading to a lower actual amount of the catalyst working in the photocatalysis.

The photocatalytic activities of three different proportions of TiO_2@BF doped with N (N_TiO_2@BF), Fe (Fe_TiO_2@BF) and Zn (Zn_TiO_2@BF) were evaluated as shown in Fig. 7(b–d), which show that when the doping ratios of N, Fe and Zn were 8%, 0.3% and 2%, respectively, the degradation effects of RhB under UV light for 3 hours were the best, reaching 47.40%, 48.20% and 60.45%, respectively. The reason why the

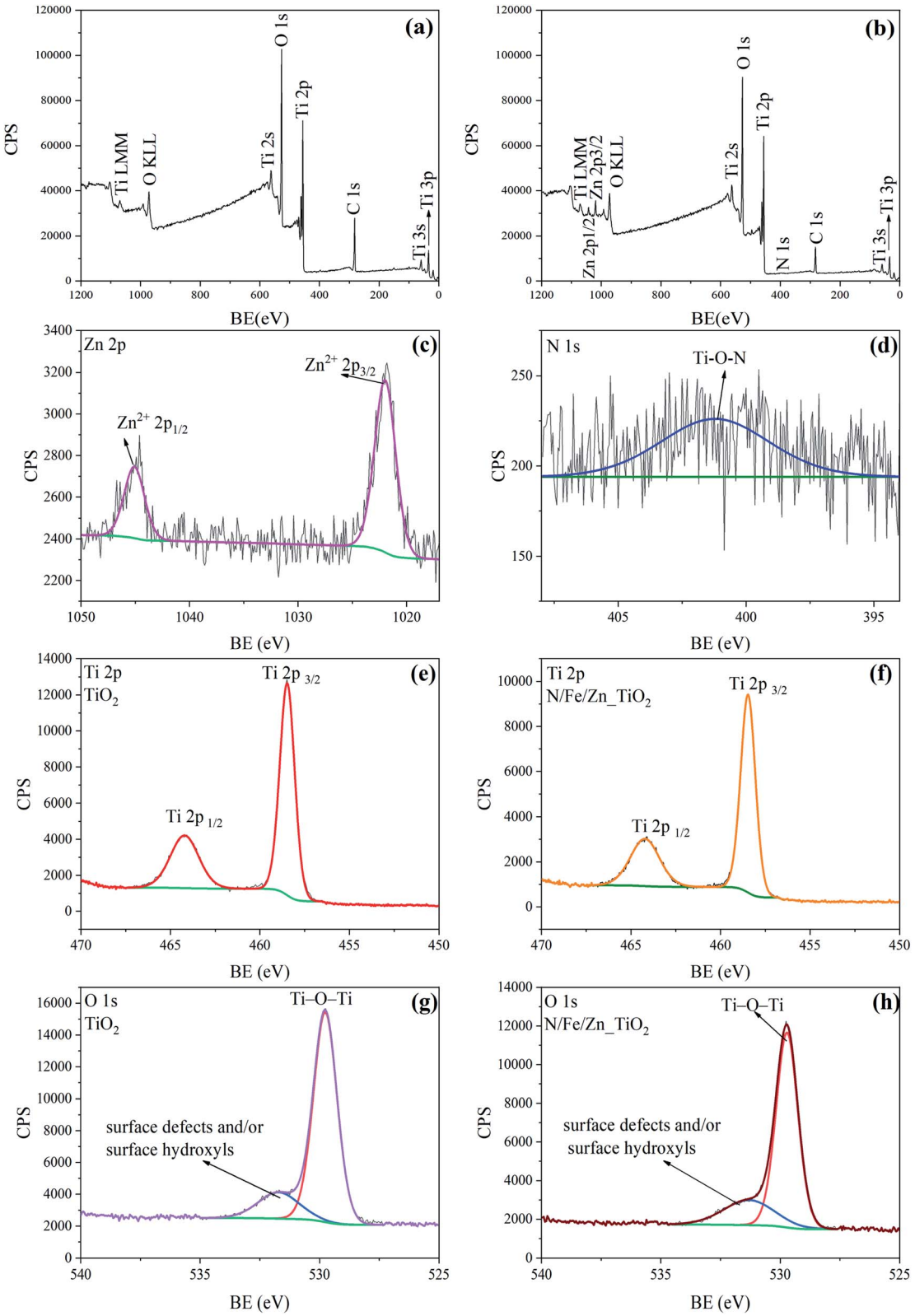

Fig. 5 XPS surface analysis for TiO_2@BF and N/Fe/Zn_TiO_2@BF: (a) TiO_2@BF full XPS spectrum, (b) N/Fe/Zn_TiO_2@BF full XPS spectrum, (c) Zn 2p core level spectra of N/Fe/Zn_TiO_2@BF, (d) N 1s core level spectra of N/Fe/Zn_TiO_2@BF, (e) Ti 2p core level spectra of TiO_2@BF, (f) Ti 2p core level spectra of N/Fe/Zn_TiO_2@BF, (g) O 1s core level spectra of TiO_2@BF, and (h) O 1s core level spectra of N/Fe/Zn_TiO_2@BF.

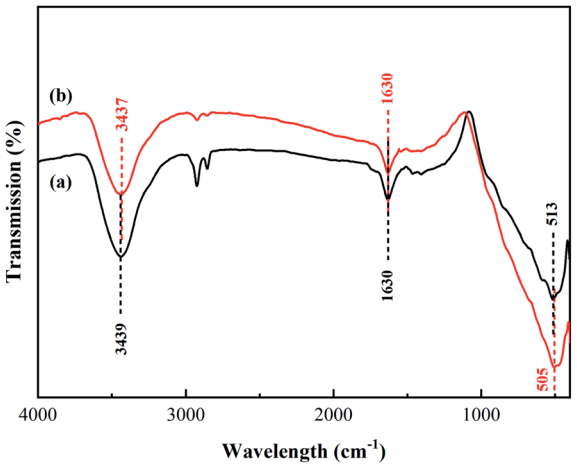

Fig. 6 FT-IR spectra of TiO_2 and N/Fe/Zn_TiO_2.

degradation efficiency of the 8% N, 0.3% Fe and 2% Zn doping ratios was higher than the 12% N, 1% Fe and 7% Zn doping ratios, respectively, might be that when the doping concentration was too high, the doping substance could not easily enter the TiO_2 lattice but instead gathered on the TiO_2 surface, reducing the active sites.

Fig. 7(e) illustrates that the adsorption/desorption equilibrium was reached in 30 min. As shown in Fig. 7(f), the photocatalytic activities of N_TiO_2@BF, Fe_TiO_2@BF, and Zn_TiO_2@BF on RhB degradation were all better than that of TiO_2@BF under UV light. In particular, the degradation efficiency of RhB by N/Fe/Zn_TiO_2@BF as the photocatalytic material was the best (67.67%), 4.33 times that of TiO_2@BF, indicating that N, Fe and Zn element doping enhanced the photocatalytic degradation effect, which was consistent with the UV-vis/DRS characterization analysis results.

Fig. 7(g) shows that the photocatalytic degradation of RhB by 8% N_TiO_2@BF, 0.3% Fe_TiO_2@BF, 2% Zn_TiO_2@BF and N/Fe/Zn_TiO_2@BF conformed to a quasi-first-order kinetic equation. The degradation rate constant (k) of RhB in different processes and the TiO_2 loading amounts for each sample are listed in Table 1. It was found that $k_{8\%N\_TiO_2@BF} < k_{0.3\%\ Fe\_TiO_2@BF} < k_{2\%\ Zn\_TiO_2@BF}$, and the k value of one element dopant of TiO_2@BF was greater than the k value of TiO_2@BF but less than the k value of N/Fe/Zn_TiO_2@BF. The degradation rate constant of N/Fe/Zn_TiO_2@BF was 7.04 times that of TiO_2@BF, indicating that doping indeed accelerated charge transfer and effectively improved the photocatalytic activity. The analysis result of XRD and RAMAN that the crystallite sizes of N/Fe/Zn_TiO_2 were smaller than TiO_2 was consistent with this photocatalytic performance.

In order to estimate the reusability and stability of N/Fe/Zn_TiO_2@BF for RhB removal, three recycling tests were conducted at the same experimental conditions. As shown in Fig. 7(h), the degradation effects of RhB were 67.67%, 55.70% and 55.84% in three consecutive cycle experiments, suggesting that N/Fe/Zn_TiO_2@BF could maintain relative stability after the first cycle experiment.

3.3 Degradation mechanism analysis

3.3.1 Optical characteristics and electronic band gaps analysis of the synthesized photocatalyst. As shown in Fig. 8, the optical characteristics and electronic band gaps of TiO_2 and G_TiO_2 were evaluated by using UV-vis diffuse reflectance. There was an obvious red shift of the absorption band for the N/Fe/Zn_TiO_2 photocatalyst compared to TiO_2. From the Tauc plot using the Kubelka–Munk function (Fig. 8 inset), the electronic band gaps of the synthesized photocatalysts were in the following order: N/Fe/Zn_TiO_2 (2.80 eV) < N_TiO_2 (2.85 eV) < Zn_TiO_2 (3.03 eV) < Fe_TiO_2 (3.08 eV) < TiO_2 (3.11 eV). As a result, N/Fe/Zn_TiO_2 showed the narrowest energy band gap (2.8 eV) compared to the other synthesized photocatalysts, which meant it was easier to generate electronic transitions under the excitation of UV light, indicating that co-doping of the N, Fe, and Zn elements in this study could have a synergistic effect and improve the photocatalytic activity of N/Fe/Zn_TiO_2.

3.3.2 Reactive species quenching experiments. To better elucidate the mechanism of N/Fe/Zn_TiO_2@BF for the degradation of rhodamine B, different reactive species quenching experiments were systemically conducted, and the results are presented in Fig. 9. In these experiments, 1.4-benzoquinone (BQ), *tert*-butyl alcohol (TBA) and EDTA-2Na were used as scavengers,[45,46] which had different affinities for different reactive oxygen species, such as the active superoxide radical ($^{\bullet}O_2^-$), hydroxyl radicals($^{\bullet}OH$) and holes (h^+). It was observed that the degradation effect of RhB (8.33%) was obviously inhibited by the EDTA-2Na scavenger, which indicated that h^+ played a crucial role in this photocatalytic degradation process. When BQ and TBA were added, respectively, the degradation rate of RhB also decreased, suggesting that $^{\bullet}OH$ and $^{\bullet}O_2^-$ have an impact on RhB removal. Herein, RhB removal during the treatment process with the BQ scavenger was different from its expected degradation trend. The reason for this result was that some dark colored degradation products of BQ had a positive effect on the determination of RhB by the spectrophotometer method, causing the measured absorbance value to become higher (Fig. 9 inset).

According to the results of the reactive species quenching experiments, it could be inferred that the h^+ active species played a dominant role, while $^{\bullet}O_2^-$ and $^{\bullet}OH$ were the minor radicals in this photocatalytic system. When N/Fe/Zn_TiO_2@BF was illuminated by UV light, electrons (e^-) in the valence band (VB) were excited to the conduction band (CB), leaving holes (h^+) in the VB, which could directly participate in the RhB degradation (eqn (3) and (4)). Meanwhile, the accumulated e^- could capture O_2 to obtain $^{\bullet}O_2^-$ (eqn (5)), which could capture H^+ generated by the ionization of H_2O to form H_2O_2, and the generated $^{\bullet}OH$ might cause the translation of the H_2O_2 (eqn (7)–(9)).[47] The $^{\bullet}O_2^-$ and $^{\bullet}OH$ radicals are capable of destroying organic compounds (eqn (6) and (10)).

$$\text{N/Fe/Zn\_TiO}_2\text{@BF} + h\nu \rightarrow e^- + h^+ \quad (3)$$

$$h^+ + \text{RhB} \rightarrow \text{degradation} \quad (4)$$

$$e^- + O_2 \rightarrow {}^{\bullet}O_2^- \quad (5)$$

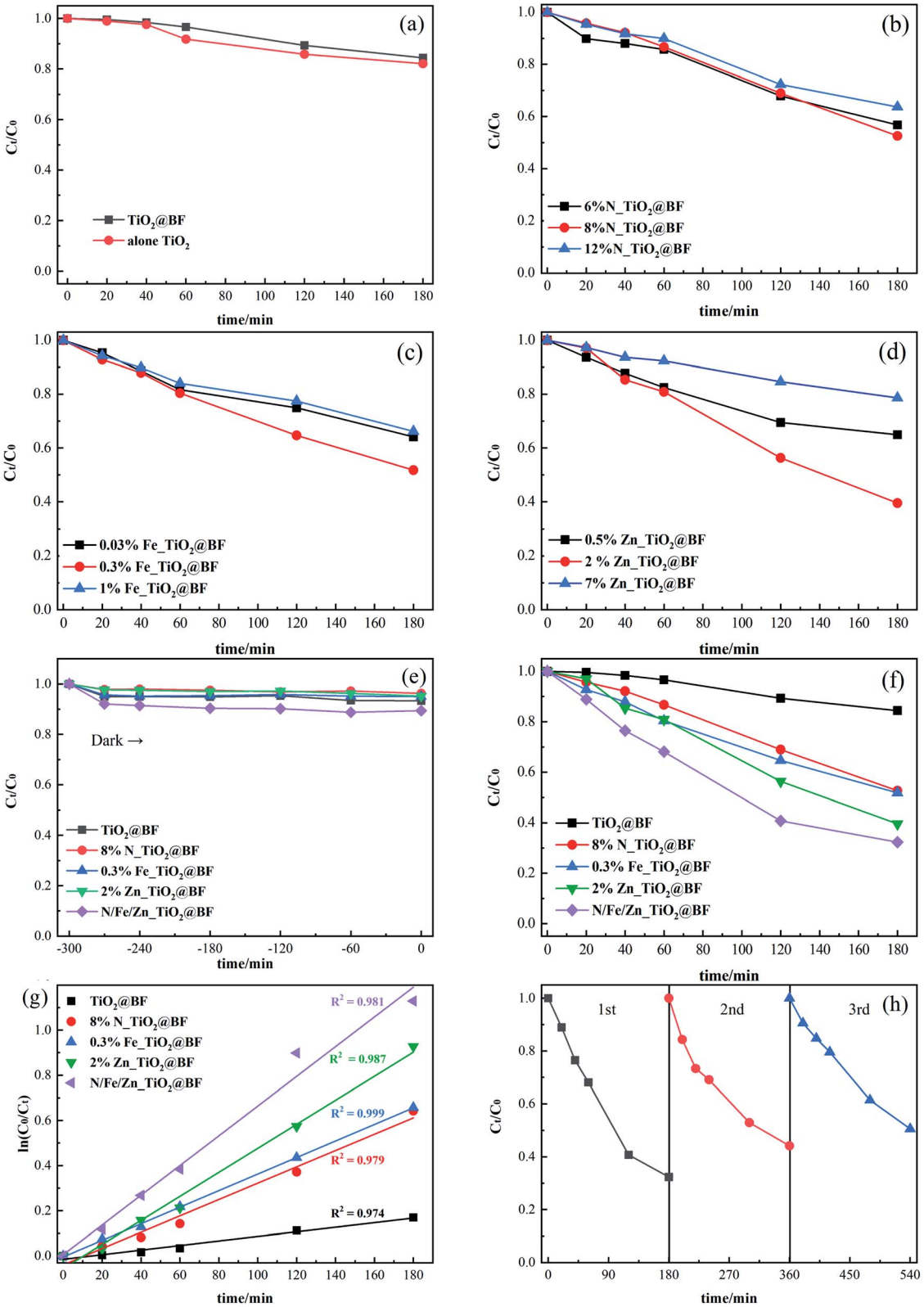

Fig. 7 (a) Photocatalytic activity of the same amount of TiO_2 without loading on BF and TiO_2@BF, (b–d, f) photocatalytic activities (in the degradation of RhB) of TiO_2@BF and G_TiO_2@BF doped with different substances at different doping ratios, (e) dark adsorption curves, (g) photocatalytic degradation kinetics and (h) the stability and reusability tests of N/Fe/Zn_TiO_2@BF for RhB removal.

Table 1 The photo-degradation rate constant and TiO_2 loading amounts of different samples

Sample	Doping ratio	$k \times 10^{-3}$ (min^{-1})	TiO_2 loading amount (mg cm^{-2})
TiO_2@BF	—	0.95	3.02
N_TiO_2@BF	6.00%	3.07	3.11
	8.00%	3.59	3.08
	12.00%	2.50	3.08
Fe_TiO_2@BF	0.03%	2.63	3.02
	0.30%	3.54	3.02
	1.00%	2.34	3.06
Zn_TiO_2@BF	0.50%	2.73	3.13
	2.00%	4.86	3.15
	7.00%	1.33	3.08
N/Fe/Zn_TiO_2@BF	—	6.69	3.04

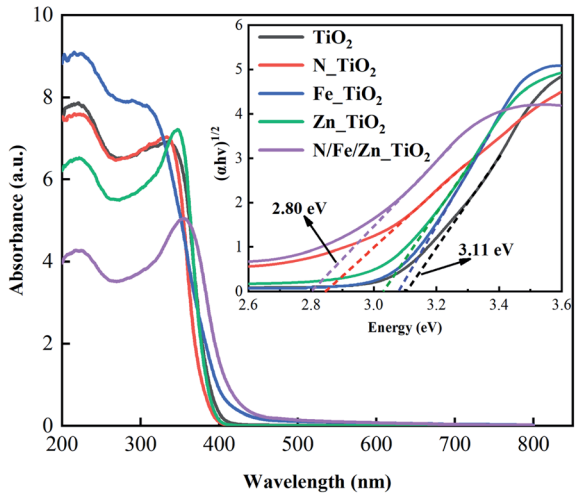

Fig. 8 UV-vis diffuse reflectance spectra of different materials (inset is the band energy spectra).

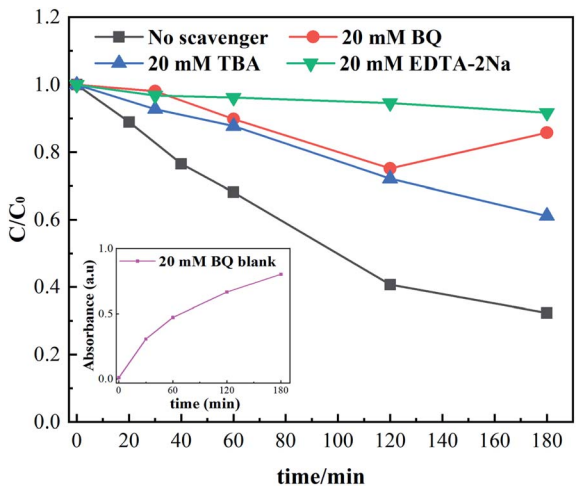

Fig. 9 Photocatalytic activities (in the degradation of RhB) of N/Fe/Zn_TiO_2@BF under the condition of different quenchers (inset is the curve of absorbance and reaction time of the 20 mM BQ without RhB and catalysts).

$$^{\bullet}O_2^- + RhB \rightarrow degradation \quad (6)$$

$$H_2O \rightarrow H^+ + OH^- \quad (7)$$

$$^{\bullet}O_2^- + 2H^+ + e^- \rightarrow H_2O_2 \quad (8)$$

$$H_2O_2 + e^- \rightarrow OH^- + {}^{\bullet}OH \quad (9)$$

$$^{\bullet}OH + RhB \rightarrow degradation \quad (10)$$

4 Conclusions

The N/Fe/Zn_TiO_2@BF composites were synthesized by a combined sol–gel calcination method. N_TiO_2@BF, Fe_TiO_2@BF, Zn_TiO_2@BF and N/Fe/Zn_TiO_2@BF exhibited higher photoactivity towards the degradation of RhB under UV light irradiation compared to TiO_2@BF. The degradation efficiency for RhB of N/Fe/Zn_TiO_2@BF was 4.3 times that of TiO_2@BF, and the degradation process of N/Fe/Zn_TiO_2@BF was consistent with first-order kinetics with a k value 7.04 times that of TiO_2@BF. The improved photoactivity was attributed to the synergistic effect of the N, Fe and Zn co-doping. The crystallite size of N/Fe/Zn_TiO_2 was only 10.4 nm, while that of TiO_2 without doping was 18.1 nm. There were more catalytic activity points with the specific surface area of N/Fe/Zn_TiO_2@BF increasing greatly, resulting in the improved catalytic efficiency. The results of the EDS, XRD, RAMAN, XPS and FT-IR analysis indicated that the elements of N, Fe and Zn were doped into the crystal lattice of TiO_2 without changing the anatase crystalline phase. In addition, N/Fe/Zn_TiO_2@BF gained a narrower energy band gap (2.80 eV), which improved the photocatalytic activity. Reactive species quenching experiments indicated that h^+ was the most important reactive species and $^{\bullet}OH$ and $^{\bullet}O_2^-$ played minor roles for the N/Fe/Zn_TiO_2@BF photocatalysis processes in the degradation of RhB.

Conflicts of interest

The authors declare that they have no known competing financial interests or personal relationships that could have appeared to influence the work reported in this paper.

Acknowledgements

This work was supported by the Major Scientific and Technological Special Program of Sichuan Province, China (2018SZDZX0027 and 2019YFS0505) and the Major Science and Technology Application Project of Chengdu City, Sichuan Province, China (2019-YF09-00081-SN).

References

1 K. Wetchakun, N. Wetchakun and S. Sakulsermsuk, *J. Ind. Eng. Chem.*, 2019, **71**, 19–49.
2 L. Jiang, X. Hu, D. Yin, H. Zhang and Z. Yu, *Chemosphere*, 2011, **82**, 822–828.
3 K. Lei, Y. Zhu, W. Chen, H. Pan, Y. Cao, X. Zhang and B. Guo, *Environ. Int.*, 2019, **130**, 104919.
4 A. M. Voigt, P. Ciorba, M. Döhla, M. Exner, C. Felder, E. Sib, D. Skutlarek, R. M. Schmithausen and H. A. Faerber, *Int. J. Hyg. Environ. Health*, 2020, **224**, 113449.
5 P. S. Basavarajappa, S. B. Patil, N. Ganganagappa, K. R. Reddy, A. V. Raghu and C. V. Reddy, *Int. J. Hydrogen Energy*, 2020, **45**, 7764–7778.
6 J. Zhang, B. Tang and G. Zhao, *Appl. Catal., B*, 2020, **279**, 119364.
7 C. Hao, Y. Xu, M. Bao, X. Wang, H. Zhang and T. Li, *J. Mater. Sci.: Mater. Electron.*, 2017, **28**, 3119–3127.
8 X. Ding, L. Gutierrez, J. P. Croue, M. Li, L. Wang and Y. Wang, *Chemosphere*, 2020, **253**, 126655.
9 W. Pronk, A. Ding, E. Morgenroth, N. Derlon, P. Desmond, M. Burkhardt, B. Wu and A. G. Fane, *Water Res.*, 2019, **149**, 553–565.
10 M. Zhang, F. Xiao, D. Wang, X. Xu and Q. Zhou, *Sep. Purif. Technol.*, 2017, **182**, 118–127.
11 S. Chen, N. Wang, L. Ma, T. Li, M. Willander, Y. Jie, X. Cao and Z. L. Wang, *Adv. Energy Mater.*, 2016, **6**, 1–9.
12 J. N. Liu, Z. Chen, Q. Y. Wu, A. Li, H. Y. Hu and C. Yang, *Sci. Rep.*, 2016, **6**, 1–9.
13 J. R. Kim and E. Kan, *J. Environ. Manage.*, 2016, **180**, 94–101.
14 F. A. El-Gohary and G. Kamel, *Ecol. Eng.*, 2016, **94**, 268–274.
15 T. H. Kim, G.-M. Go, H.-B. Cho, Y. Song, C.-G. Lee and Y.-H. Choa, *Front. Chem.*, 2018, **6**, 1–10.
16 Y. Yan, W. Shi, Z. Yuan, S. He, D. Li, Q. Meng, H. Ji, C. Chen, W. Ma and J. Zhao, *J. Am. Chem. Soc.*, 2017, **139**, 2083–2089.
17 H. Zong, T. Zhao, G. Zhou, R. Qian, T. Feng and J. H. Pan, *Catal. Today*, 2019, **335**, 252–261.
18 A. R. Khataee and M. B. Kasiri, *J. Mol. Catal. A: Chem.*, 2010, **328**, 8–26.
19 Y. N. Li, Z. Y. Chen, M. Q. Wang, L. zhen Zhang and S. J. Bao, *Appl. Surf. Sci.*, 2018, **440**, 229–236.
20 L. Kong, Z. Jiang, C. Wang, F. Wan, Y. Li, L. Wu, J. F. Zhi, X. Zhang, S. Chen and Y. Liu, *ACS Appl. Mater. Interfaces*, 2015, **7**, 7752–7758.
21 J. Wen, X. Li, W. Liu, Y. Fang, J. Xie and Y. Xu, *Chin. J. Catal.*, 2015, **36**, 2049–2070.
22 L. Pan, J. J. Zou, X. Zhang and L. Wang, *J. Am. Chem. Soc.*, 2011, **133**, 10000–10002.
23 J. B. Priebe, J. Radnik, A. J. J. Lennox, M. M. Pohl, M. Karnahl, D. Hollmann, K. Grabow, U. Bentrup, H. Junge, M. Beller and A. Brückner, *ACS Catal.*, 2015, **5**, 2137–2148.
24 R. Zanella, E. Avella, R. M. Ramírez-Zamora, F. Castillón-Barraza and J. C. Durán-Álvarez, *Environ. Technol.*, 2018, **39**, 2353–2364.
25 S. Luan, D. Qu, L. An, W. Jiang, X. Gao, S. Hua, X. Miao, Y. Wen and Z. Sun, *Sci. Bull.*, 2018, **63**, 683–690.
26 R. Lu, Y. Wei, C. Chen and T. Wu, *J. Alloys Compd.*, 2019, **790**, 99–108.
27 Y. Xiao, X. Sun, linyu Li, J. Chen, S. Zhao, C. Jiang, L. Yang, L. Cheng and S. Cao, *Chin. J. Catal.*, 2019, **40**, 765–775.
28 A. Mishra, A. Mehta, S. Kainth and S. Basu, *J. Alloys Compd.*, 2018, **764**, 406–415.
29 E. Rezaei, R. Azar, M. Nemati and B. Predicala, *J. Environ. Chem. Eng.*, 2017, **5**, 5902–5911.
30 A. Buzarovska, C. Gualandi, A. Parrilli and M. Scandola, *Composites, Part B*, 2015, **81**, 189–195.
31 J. M. Wu and Q. E. Zhao, *Appl. Surf. Sci.*, 2020, **527**, 146779.
32 W. Li and T. Zeng, *PLoS One*, 2011, **6**, 2–7.
33 K. H. Leong, P. Monash, S. Ibrahim and P. Saravanan, *Sol. Energy*, 2014, **101**, 321–332.
34 T. Ohsaka, *J. Phys. Soc. Jpn.*, 1980, **48**, 1661–1668.
35 H. C. Choi, Y. M. Jung and S. Bin Kim, *Vib. Spectrosc.*, 2005, **37**, 33–38.
36 H. W. Cho, K. L. Liao, J. S. Yang and J. J. Wu, *Appl. Surf. Sci.*, 2018, **440**, 125–132.
37 Y. Kim, J. Lee, H. Jeong, Y. Lee, M. H. Um, K. M. Jeong, M. K. Yeo and M. Kang, *J. Ind. Eng. Chem.*, 2008, **14**, 396–400.
38 P. Bharathi, M. Krishna Mohan, V. Shalini, S. Harish, M. Navaneethan, J. Archana, M. Ganesh Kumar, P. Dhivya, S. Ponnusamy, M. Shimomura and Y. Hayakawa, *Appl. Surf. Sci.*, 2020, **499**, 143857.
39 X. Cheng and L. Yang, *Arabian J. Chem.*, 2016, **9**, S1706–S1711.
40 M. Sreedhar, I. N. Reddy, P. Bera, D. Ramachandran, K. Gobi Saravanan, A. M. Rabel, C. Anandan, P. Kuppusami and J. Brijitta, *Appl. Phys. A: Mater. Sci. Process.*, 2015, **120**, 765–773.
41 M. Sreedhar, I. Neelakanta Reddy, C. V. Reddy, J. Shim and J. Brijitta, *Mater. Sci. Semicond. Process.*, 2018, **85**, 113–121.
42 X. Wang, F. Wang, C. Bo, K. Cheng, J. Wang, J. Zhang and H. Song, *Appl. Surf. Sci.*, 2018, **453**, 320–329.
43 L. Ma, I. Jia, X. Guo and L. Xiang, *Chin. J. Catal.*, 2014, **35**, 108–119.
44 Z. He, W. Que, J. Chen, Y. He and G. Wang, *J. Phys. Chem. Solids*, 2013, **74**, 924–928.
45 W. Wang, Z. Zeng, G. Zeng, C. Zhang, R. Xiao, C. Zhou, W. Xiong, Y. Yang, L. Lei, Y. Liu, D. Huang, M. Cheng, Y. Yang, Y. Fu, H. Luo and Y. Zhou, *Chem. Eng. J.*, 2019, **378**, 122132.
46 R. Li, M. Cai, Z. Xie, Q. Zhang, Y. Zeng, H. Liu, G. Liu and W. Lv, *Appl. Catal., B*, 2019, **244**, 974–982.
47 W. Wang, Q. Niu, G. Zeng, C. Zhang, D. Huang, B. Shao, C. Zhou, Y. Yang, Y. Liu, H. Guo, W. Xiong, L. Lei, S. Liu, H. Yi, S. Chen and X. Tang, *Appl. Catal., B*, 2020, **273**, 119051.